Finite element analysis of gas bearings for oil-free turbomachinery

Luis San Andrés, Deborah Wilde

Turbomachinery Laboratory, Mechanical Engineering Department
Texas A&M University
College Station, TX 77843-3123, USA

ABSTRACT. *Further advancements in high performance turbomachinery operating at extreme temperatures mandate the development of gas film bearing technology to procure compact units with improved efficiency in an oil-free environment. A novel finite element (FE) procedure to model thin film gas bearings follows. The FE model incorporates a novel class of high order shape functions ensuring computational efficiency and numerical stability even at (infinity) high speed bearing numbers. The method does not rely on cumbersome schemes for evaluation of advection flow terms in the Reynolds equation nor introduces artificial diffusion into the numerical solution. A computational FE program forwards predictions for the static performance and dynamic force coefficients of an externally pressurized gas bearing for ready application to an automotive turbocharger. The predictions show the strong effects of excitation frequency on the dynamic force coefficients and the onset of a hydrodynamic instability at moderately low rotor speeds. The analysis of predictions evidences the benefits and limits of rigid surface gas bearings for oil-free turbomachinery.*

RÉSUMÉ. *Les futures avancées technologiques concernant les turbomachines à haute performance opérant à d'extrêmes températures obligent au développement de la technologie des paliers à gaz afin d'obtenir des unités compactes à l'efficacité améliorée dans un environnement sans huile. Une nouvelle procédure par éléments finis (EF) est présentée dans cet article. Le modèle EF incorpore une nouvelle classe de fonctions de forme d'ordre élevé assurant l'efficacité du calcul et la stabilité numérique même à nombres de vitesse élevé (infini) pour le palier. La méthode ne repose pas sur d'encombrants schémas numériques pour l'évaluation des termes de l'écoulement par advection dans l'équation de Reynolds et n'introduit pas non plus de diffusion artificielle dans la solution numérique. Un programme de calculs EF donne des prédictions pour les performances statiques et les coefficients de force dynamique d'un palier à gaz à pressurisation externe pour l'application directe à un turbocompresseur automobile. Les prédictions montrent les effets importants de la fréquence d'excitation sur les coefficients de force dynamique et la limite de stabilité hydrodynamique à vitesse de rotation modérée. L'analyse de ces prédictions met en évidence les avantages et les limites des paliers à gaz à surface rigide pour les turbomachines fonctionnant sans huile.*

KEY WORDS: *gas bearings, rotordynamics, stability, finite element model*

MOTS-CLÉS : *paliers à gaz, dynamique du rotor, stabilité, modèle éléments finis*

1. Introduction

Gas turbines and turbochargers currently use oil lubricated rolling element and fluid film bearings as rotor support elements providing adequate stiffness and damping for vibration dissipation and mount isolation with fractional power losses. However, strict environmental concerns and further needs for low emissions and improved efficiencies mandate the development of proven gas film bearings to procure compact units in an oil-free environment. Eliminating the requirement for oil lubrication can also reduce all the plumbing, scavenging and sealing, lessen weight and complexity, and improve reliability.

Current research thus focuses on the development of computational mechanic models, validated by relevant experimental results, to demonstrate the reliability and limitations of gas bearings for implementation in high performance oil-free turbomachinery. The operating characteristics include exceedingly high speeds, minute film clearances, with the process fluid (air or gas) at relatively low pressures relative to ambient. Foil gas bearings are a certain configuration, proven successful in micro power systems. However, their proprietary nature, high initial high cost and lack of (published) analyses and manufacturing process prevents the widespread deployment into competitive turbomachinery markets, such as in automotive turbochargers, for example. For this application, inexpensive rigid surface gas bearings with an appropriate coating on the rotor to reduce drag friction and limit wear on start up and shut down cycles are being considered as viable alternatives.

The archival literature shows copious analyses for gas bearings with early applications of grooved bearings and seals to gyroscopic (positioning) systems and buffer gas sealing arrangements [GRO 62, HAM 94]. Later advances detail improved numerical procedures for expedient analysis and design encompassing operating speed regions on which the character of the flow nonlinear (Reynolds) equation changes from elliptic to parabolic.

Fuller [FUL 69] reviews the major advances in gas bearing modeling appearing in the 1960's. Since then, several techniques for the efficient numerical solution of Reynolds equation and analyses addressing the major issue of rotor-bearing stability have evolved. Castelli and Pirvics [CAS 68] introduce block solvers for finite difference models, and Castelli and Elrod [CAS 65] forward the perturbation method for linearization of Reynolds equation and evaluation of fluid film reaction forces due to small amplitude motions about an equilibrium state. Castelli and Elrod [CAS 65], and Elrod, McCabe and Chu [ELR 67] implement the orbit and step-jump methods for fast evaluation of the nonlinear equations of motion governing the dynamic response of a rotor supported on gas bearings. The analyses go beyond the limits of the perturbation model, which cannot represent the strong non linearities and self-excited instabilities apparent in gas bearings.

Design charts for prediction of the performance and stability conditions in simple hydrodynamic and hydrostatic gas bearings are readily available. Elrod and Malanoski [ELR 60], Lund [LUN 68], Gunter et al. [GUN 64], and Castelli and Vohr [CAS 67] present graphical results for plain cylindrical and lobed bearings, tilting pad

bearings and herringbone configurations, respectively. Lund [LUND 64] also advances the first approximate analysis and results for hybrid (hydrostatic / hydrodynamic) gas bearings. Recently, Czolczynski [CZO 96] using the orbit method reports dynamic force coefficients representative of a full period of motion in a simple rotor-gas bearing configuration. Note that the design charts displaying static performance and dynamic force coefficients for gas bearings are limited to either centered journal operation, or low surface speeds (small compressibility numbers), or external pressurization with a large number of feed orifices.

Fixed geometry gas bearings are prone to show a (self-excited) hydrodynamic instability at sufficiently large operating speeds. Hydrostatic pressurization brings forward a characteristic pneumatic hammer that more severely limits the safe range of rotor speeds, feed pressures and excitation frequencies where gas bearings remain stable (Majumder and Majumdar [MAJ 88], and Lund [LUN 67]). Pneumatic hammer, characterized by a sudden loss of damping even at low frequency excitations, is controlled by the flow-versus-pressure time lag in the gas supply restrictors. Inherent type orifices, i.e. a feed condition with no trapped gas volumes, alleviate the problem at the expense of decreasing the bearing load capacity.

Presently, a FE computational analysis for high-speed gas bearings including external orifice pressurization follows. FE procedures in gas lubrication are generally based on either the Galerkin or the Petrov-Galerkin weighted residual methods. The Galerkin method demands fine meshes to provide stable numerical solutions for operating conditions with large bearing speed (compressibility) numbers. The Petrov-Galerkin FEM method is efficient and stable at high speed numbers, although it requires of ad-hoc procedures, such as upwinding, for modeling the advection flow terms in the Reynolds equation [HEI 77]. Faria and San Andrés [FAR 00] introduce a set of high order shape (weight) functions to overcome the numerical limitations and need of special integration procedures in the classical techniques. The family of high order interpolation functions is analytically obtained from an approximate solution to the Reynolds equation within an element domain.

Numerical predictions for the static performance and dynamic force coefficients for a three pad hybrid gas bearing follow as a function of journal speed. The bearing geometry and operating conditions reproduce those found in an existing commercial automotive turbocharger. The predictions evidence the importance of excitation frequency on the dynamic force coefficients and their ultimate effect on the rotordynamics of high speed rotors supported on air bearings, including regions of unstable response with potentially harmful subsynchronous motions.

2. Analysis

Figure 1 shows a characteristic hybrid (hydrostatic/hydrodynamic) gas bearing composed of a number of bearing pads, each with one or more feed orifices for external pressurization. The journal rotates at an angular speed (ω) and the displacements (e_X, e_Y) denote its position within the bearing clearance. The film geometry is described relative to the coordinate system ($x=R\theta$, y) located on the

bearing plane. A pad extends from Q_l to Q_t, the leading edge and trailing edges, respectively, and Q_p is the pad offset angle. The pad film thickness is given by

$$h = C - r_p \cos(q - Q_p) + e_X(t)\cos q + e_Y(t)\sin q = H C \qquad [1]$$

where C and r_p are the nominal clearance and pad preload, respectively.

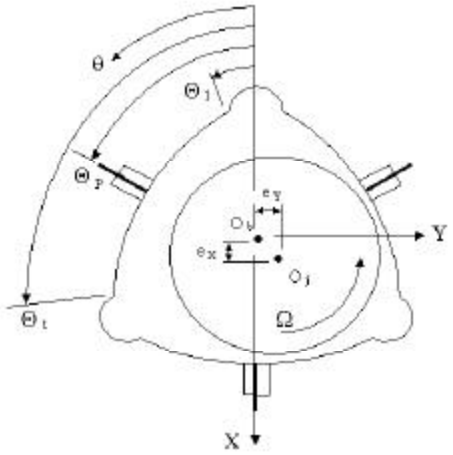

Figure 1. *Geometry of hydrostatic / hydrodynamic gas bearing.*

In an ideal gas undergoing an isothermal process, the density and pressure are related by $r = \frac{P}{\Re_g \cdot T}$, with $\Re_g$ and T representing the gas constant and operating temperature, respectively. The compressible fluid Reynolds equation describes the inertialess and isoviscous flow within the thin film. This equation establishes the balance of pressure and shear driven mass flow rates and the mass flow rate ($\dot{m}_{OR}$) from an external pressure source, i.e.

$$\nabla \cdot \left(\frac{-h^3 P}{12m} \cdot \nabla(P) \right) + \frac{W \cdot R}{2} \cdot \frac{\partial}{\partial x}(Ph) + \frac{\partial}{\partial t}(Ph) = \frac{(\Re_g T) \cdot \dot{m}_{OR}}{A} \qquad [2]$$

In the analysis, the pressure is ambient (P_a) on the sides of a bearing pad. Dimensionless coordinates, film thickness and pressures are defined as

$$\bar{x}=\frac{x}{L_x},\qquad \bar{y}=\frac{y}{L_x},\qquad t=w\,t,\qquad H=\frac{h}{C},$$
$$p=\frac{P}{P_*},\qquad \bar{p}=\frac{P}{P_s}=\frac{p}{p_s},\qquad p_a=\frac{P_a}{P_*/C},\qquad \bar{p}_a=\frac{P_a}{P_s/C}=\frac{p_a}{p_s/C} \qquad [3]$$

where $P_* = P_a$ is a characteristic pressure, and $L_x = R(Q_t - Q_l)$ is the pad circumferential length.

The feed source mass flow rate ($\dot{m}_{OR}$) is a function of the pressure ratio $\bar{P}$ =P/P_s and the orifice geometry, see Figure 2, i.e.

$$\dot{m}_{OR} = F \cdot m(\bar{p}) \cdot g(H), \text{ with } F = \sqrt{\Re_g T}\,\frac{p\ a^2}{A}P_s \qquad [4]$$

and

$$m(\bar{P}) = \begin{cases} \left(2\cdot\frac{k}{k+1}\right)^{1/2}\cdot\left(\frac{2}{k+1}\right)^{1/k-1} & for \quad \bar{P} < \bar{P}_{choke},\ \ \bar{P}_{choke}=\left(\frac{2}{k+1}\right)^{k/k-1} \\ a'\cdot\left(2\cdot\frac{k}{k-1}\right)^{1/2}\cdot\bar{P}^{1/k}\cdot\left(1-\bar{P}^{k-1/k}\right)^{1/2} & for \quad \bar{P} > \bar{P}_{choke} \end{cases} \qquad [5]$$

where k is the gas specific heat ratio, and (a') is a non-isentropic loss coefficient. The function

$$g(H)=\frac{H}{(H^2+D^2)^{1/2}},\ D=\frac{a^2}{d\cdot C} \qquad [6]$$

defines the characteristics of the feed source. Most externally pressurized gas bearings are designed with inherent feed restrictors to avoid pneumatic hammer effects. In this case, the pressure drop occurs at the curtain area ($p\ d\ h$), and thus the geometric ratio $D>>1$ renders $g = dh/a^2$.

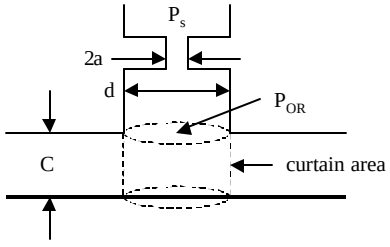

Figure 2. *Geometry of feed orifice in gas bearing.*

Consider small amplitude journal motions (De_X, De_Y) of frequency (w) about an equilibrium position (e_{X_0}, e_{Y_0}), i.e. $e_a \cong e_{a0} + De_a e^{iw\cdot t}{}_{,a=X,Y}$. The journal dynamic motions cause corresponding perturbations in film thickness and pressure about an equilibrium or zeroth-order field (h_0, P_0). Thus,

$$h = HC = h_0 + De_a\ f_a e^{iw\cdot t}\ ;\ {}_{a=X,Y}\ ;\ f_X = \cos q;\ f_Y = \sin q \qquad [7.a]$$

$$P = P_0 + De_a P_a e^{iw\cdot t} \qquad [7.b]$$

Substitution of equations [7] into Reynolds equation [2] leads to the zeroth- and first-order (dimensionless) equations for the equilibrium and perturbed pressure fields, i.e.

$$\left[-\frac{\partial}{\partial \bar{x}}\left(p_0 H_0^3 \frac{\partial p_0}{\partial \bar{x}}\right) - \frac{\partial}{\partial \bar{y}}\left(p_0 H_0^3 \frac{\partial p_0}{\partial \bar{y}}\right)\right] + L\frac{\partial}{\partial \bar{x}}(p_0 H_0) = d_{OR}\cdot\left[m(\bar{p}_0)\cdot g(H_0)\right] \qquad [8]$$

and

$$\begin{aligned} -\frac{\partial}{\partial \bar{x}}\cdot\left(H_0{}^3\frac{\partial}{\partial \bar{x}}(p_0 p_a) + 3H_0{}^2 p_0 f_a\cdot\frac{\partial}{\partial \bar{x}}p_0\right) - \frac{\partial}{\partial \bar{y}}\cdot\left(H_0{}^3\frac{\partial}{\partial \bar{y}}(p_0 p_a) + 3H_0{}^2 p_0 f_a\cdot\frac{\partial}{\partial \bar{y}}p_0\right) \\ + L\frac{\partial}{\partial \bar{x}}(p_0 f_a + p_a H_0) + s\cdot i\cdot(p_0 f_a + p_a H_0) = \\ d_{OR}\left[m(\bar{p}_0)\cdot g(H_0)\right]\cdot\left\{\left[\left[\frac{2-(1+k)\bar{p}_0^g}{2\left(1-\bar{p}_0^g\right)k}\right]\bar{P}_a\right] + \left[\left\{\frac{1}{H_0\left[1+\frac{H_0^2}{D^2}\right]}\right\}f_a\right]\right\} \end{aligned} \qquad [9]$$

where $L = \dfrac{6mWRL_x}{C^2 P_*}$, $s = \dfrac{12mw\ L_x^2}{C^2 P_*}$, and $d_{OR} = \dfrac{p\ a^2}{A}\dfrac{12mL_x^2}{C^3(P_* r_*)^{1/2}}\ p_s$ [10]

are the speed (or compressibility) and frequency numbers, and feed orifice parameter, respectively[1]. $\{p_0 = 1, (p_a = 0)_{a=X,Y}\}$ at the pad boundaries. Fluid film reaction forces (F_X, F_Y) for each pad are defined as

[1] Equation [9] is strictly valid for unchoked flow through the feed orifice.

$$F_a = \int_0^L \int_q (P - P_a) f_a \, R \, dq \, dy = F_{a_0} - Z_{ab} \, De_a e^{\mathbf{i}wt} \; ; \quad {}_{a,b=X,Y} \qquad [11]$$

The real and imaginary parts of the impedance functions (Z_{ab}) define the stiffness and damping coefficients $\{K_{ab}, C_{ab}\}_{a,b=X,Y}$, i.e.

$$Z_{ab} = K_{ab} + \mathbf{i}w \; C_{ab} = -\int_0^L \int_Q P_b \; h_a \; R \, dq \; dy \; ; \quad {}_{a,b=X,Y} \qquad [12]$$

Note that fluid compressibility renders frequency dependent force coefficients. Bearing reaction forces and force coefficients are obtained by summation of the components from each pad.

3. Finite element model

The flow domain in a pad is divided into four-noded rectangular finite elements $W_e : \left\{ l_x^e = \frac{1}{N_x}, l_y^e = \frac{L/L_x}{N_y} \right\}$ where (N_x, N_y) is the global number of elements in the circumferential and axial directions, respectively. Within an element the zeroth- and first-order pressures are functions of the nodal pressures and shape (weight) functions $\{y_i^e\}_{i=1..4}$, i.e.

$$p_0^e = \sum_{i=1}^4 y_i^e \, p_{0_i}^e \, , \; p_a^e = \sum_{i=1}^4 y_i^e \, p_{a_i}^e \; ; \; {}_{a=X,Y} \qquad [13]$$

These equations are substituted into [8] and [9], which are further multiplied by an identical set of weight functions and integrated over an element domain. The Petrov-Galerkin method leads to the following set of zeroth- and first-order finite element equations (not including a source of external pressurization)

$$\begin{aligned} & k_{ji}^e \, p_{0i}^e = r_j^e + q_j^e \; ; \\ & k_{a\,ji}^e \, p_{a_i}^e = r_{a_j}^e \; f_a + q_{a_j}^e \; ; \; {}_{i,j=1..4;a=X,Y} \end{aligned} \qquad [14]$$

where

$$k_{ji}^e = \iint_{W_e} \left[p_0^e \, H_0^3 \left(y_{i,\bar{x}}^e \, y_{j,\bar{x}}^e + y_{i,\bar{y}}^e \, y_{j,\bar{y}}^e \right) - L \, H_0 y_i^e \, y_{j,\bar{x}}^e \right] dW_e \, ,$$

$$r_j^e = 0 \; ; \qquad q_j^e = -\oint_{G_e} y_j^e \dot{m}_h^e \, dG_e \qquad [15]$$

and

$$k_{a\,ji}^{\ e} = \iint_{W_e} \begin{bmatrix} p_0^e H_0^3 \left(y_{i,\bar{x}}^{\ e} y_{j,\bar{x}}^{\ e} + y_{i,\bar{y}}^{\ e} y_{j,\bar{y}}^{\ e} \right) + y_i^{\ e} H_0^3 \left(p_{0,\bar{x}} y_{j,\bar{x}}^{\ e} + p_{0,\bar{y}} y_{j,\bar{y}}^{\ e} \right) \\ - L H_0 y_i^{\ e} y_{j,\bar{x}}^{\ e} + is\ H_0 y_i^{\ e} y_j^{\ e} \end{bmatrix} .dW_e$$

$$r_{a\,j}^{\ e} = - \iint_{W_e} \left[3 p_0^e H_0^2 \left(p_{0,\bar{x}} y_{j,\bar{x}}^{\ e} + p_{0,\bar{y}} y_{j,\bar{y}}^{\ e} \right) - L\, p_0 y_{j,\bar{x}}^{\ e} + is\ p_0 y_j^{\ e} \right] dW_e \quad [16]$$

$$q_{a_j}^e = - \oint_{G_e} y_j^{\ e} \dot{m}_{a\,h}^e \, dG_e \ ;$$

***[k]*^{e}** represents the element fluidity matrix, and ***(r)*^{e}** and ***(q)*^{e}** denote the vectors of shear and squeeze flows, and nodal mass fluxes ($\dot{m}_h^e$) through the element boundary G_e, respectively.

Within a finite element $W_e : \left\{ \bar{x}^e \cong \frac{(x+1)}{2} l_x^e , \bar{y}^e \cong \frac{(h+1)}{2} l_y^e \right\}$, and natural coordinates $\{x, h\} \in [-1, +1]$, the novel shape functions are: [FAR 00]

$$y_1^{\ e} = \frac{1}{2}(1-h)\left(\frac{e^{l_e} - e^{l_e x}}{e^{l_e} - e^{-l_e}} \right); \qquad y_2^{\ e} = \frac{1}{2}(1-h)\left(\frac{e^{l_e x} - e^{-l_e}}{e^{l_e} - e^{-l_e}} \right)$$

$$y_3^{\ e} = \frac{1}{2}(1+h)\left(\frac{e^{l_e x} - e^{-l_e}}{e^{l_e} - e^{-l_e}} \right); \qquad y_4^{\ e} = \frac{1}{2}(1+h)\left(\frac{e^{l_e} - e^{l_e x}}{e^{l_e} - e^{-l_e}} \right) \quad [17]$$

where $l_e = \frac{L\, l_x^e}{p_0^e H_e^2}$ is a local Peclet number showing the ratio of convection (shear) flow to diffusion (Poiseuille) flow. At low bearing speed numbers ($l_e \to 0$), the novel shape functions reduce to the well known bilinear interpolation functions [BAT 82]. For high speed numbers where fluid convection dominates the film flow, $l_e \to \infty$, the shape functions produce a full up winding fluidity matrix with negligible diffusive terms.

The novel finite element formulation eliminates the need of an upwind parameter and non-symmetrical weighting functions as in the case of the Petrov-Galerkin scheme. The upwinding effect is intrinsically contained in the “exact” functions without resort to special schemes for the advection terms. No artificial viscosity is therefore introduced into the solution. However the approximate solution within an element (*e*) depends on a good estimate for p_o^e.

Equations [14] are evaluated over the flow domain and then condensed by enforcing the corresponding boundary conditions and including the source terms arising from any external (orifice) pressurization. The resultant global set of equations is

$$[k]_G \{\overline{p}_0\}_G = \{Q_0\}_G + \{R_0\}_G \qquad [18]$$

where $[k]_G = \bigcup_{e=1}^{Nem} [k]^e$, $\{Q\}_G = \bigcup_{e=1}^{Nem} \{q\}^e + \{q\}^{sources}$, $\{R\}_G = \bigcup_{e=1}^{Nem} \{r\}^e$. The asymmetric global fluidity matrix $[k]_G$ is nonlinear since its elements depend on the zeroth-order pressure field.

An iterative procedure forwards the solution to the system of nonlinear (zeroth order) global equations [18]. Earlier developments [FAR 99, FAR 01] relied on the constant evaluation, assembly and decomposition of the global fluidity matrix. Presently, a line solver with successive under-relaxation is used. The procedure assembles the finite element equations along a line (constant axial coordinate) and solves them using the TDMA algorithm. The present method is faster than the full matrix decomposition procedure since new pressures are immediately updated in the iterative procedure. Good convergence rates are found by selecting appropriate under relaxation factors (0.7, typically).

The appendix presents FE predictions for a typical hydrodynamic gas bearing. The FE results compare exactly with published design charts from Lund [LUN 68], and extend the original predictions to very large bearing speed numbers.

4. Numerical predictions from FE model for gas bearings

Currently, there is a pressing need to develop and implement gas bearings, replacing oil-lubricated bearings, in high-speed automotive turbochargers (TC). Environmental concerns requiring lower emissions and enhancements in operating efficiency drive the technology upgrade. Note that TC manufacturers are extremely cost conscious, and thus, as a first step in the development, a drop-in bearing type replacement is considered. That is, the selected gas bearing should fit the existing rotor and casing envelope to avoid a major redesign of the turbomachinery components.

Predictions for static performance and dynamic force coefficients for a three-pad hydrostatic/hydrodynamic gas bearing configuration follow. Table 1 details the bearing geometry and operating conditions. Pressurized air bleed from the TC compressor discharge will be routed into the gas bearings through small radial orifices, two on the each pad middle plane and equally spaced at a distance (0.15 L) from the pad centerline. The orifice diameter noted is of the same magnitude as the bearing clearance, and thus proper machining procedures and adequate filtration measures need be addressed in an actual application. To avoid undesirable pneumatic hammer effects the analysis regards an inherent feed type restriction. That is, the flow restriction (pressure loss) actually occurs at the flow curtain area ($\pi d h$) since there is not a feed volume at the orifice discharge plane.

The FE bearing model uses N_x=25 circumferential and N_y =15 axial nodes to describe each pad half-geometry. Numerical calculation of the zeroth and first-order dimensionless pressure fields proceeds until convergence is achieved within a

tolerance limit of 10^{-5}, not exceeding a maximum of 500 iterations imposed as a limit to achieve the desired accuracy. Faria [FAR 99, FAR 01] details the analysis on the accuracy and convergence rate of the present FE model with extensive comparisons to predictions derived from a classical Galerkin formulation.

The turbocharger weighs approximately 0.100 kg, and thus the applied static load (W) into each bearing is about 0.5 N (half rotor weight), thus indicating a low specific pressure (W/LD) of 0.04 bar (0.57 psi). The static load, directed towards the middle of a bearing pad (X direction), is so small that the TC rotor will run near its centered position for most of the operating speed range. In fixed geometry bearings this operating condition is potentially harmful due to the onset of (one or more) sub synchronous hydrodynamic instability.

Table 1. *Three pad gas bearing: geometry and operating conditions*
Arc length: 110 °, pad offset: 50%. Ambient pressure, P_a = 1.01 bar

Length	L	13.8 mm	L/D=1.50
Diameter	D	9.20 mm	D/C_{min}=1,840
Nominal clearance	C	10 μm	
Preload	r_p	5 μm	$C_{min}= C- r_p$
Orifice diameter	d	0.0127 mm	a' = 1.0

			Air inlet temperature to compressor T=303 °K (30 °C)		
Rotor speed krpm	Pressure ratio (*)	Temperature ratio (*)	Pressure supply, P_s (bar)	Gas viscosity Pa·s x 10^{-5}	Gas density at P_a. kg/m^3
30	1.041	1.016	1.055	1.882	1.149
60	1.163	1.062	1.180	1.947	1.099
90	1.368	1.132	1.387	2.044	1.031
120	1.653	1.218	1.677	2.161	0.958
150	2.021	1.315	2.050	2.289	0.888
180	2.470	1.417	2.500	2.420	0.824

(*) Pressure and temperat ure ratios refer to compressor discharge to inlet magnitudes.

The results of the computational predictions are presented in dimensionless form. Table 2 displays the definitions for the bearing speed (or compressibility) number (L_B) and conversion factors for evaluation of dimensionless orifice flow, bearing torque, and rotordynamic force coefficients.

Figure 3 shows the specified supply pressure (P_s/P_a) and calculated orifice pressure (P_{oR}/P_a), dimensionless orifice mass flow rate and bearing drag torque as a function of the rotor speed. The figure also includes the journal eccentricity and attitude angle for the operating static load. The predictions indicate that the hydrostatic action does not initiate until the rotor reaches a speed of 75,000 rpm, since the feed pressure extracted fro m the compressor is not large enough. The orifice flow rate then increases rapidly, although its actual magnitude is rather small.

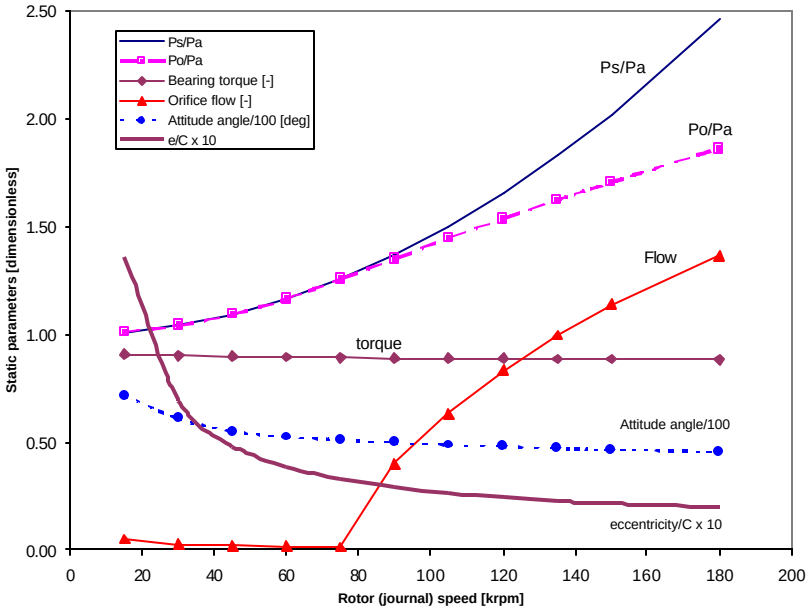

Figure 3. *Dimensionless supply and orifice pressures, orifice mass flow rate, drag torque, attitude angle and static eccentricity versus journal speed. (Load W_x= 0.5N)*

Table 2. *Bearing speed number and conversion factors for performance parameters*

Parameter	Symbol	Definition
Speed (compressibility) number	L_B	$\frac{6\,m\,L}{P_a}\left(\frac{D}{2\,c_{min}}\right)^3$
Torque	$\overline{T}_{orq} = T_{orq} / T_*$	$T_* = m\,W\,R^3\,\frac{L}{c_{min}}\,N_{pad}\,Q_P$
Orifice Mass Flow Rate	$\overline{\dot{m}}_{oR} = \dot{m}_{oR} / \dot{m}_*$	$\dot{m}_* = \frac{p\,d^2}{4}\sqrt{2\,r\,(P_s - P_a)}$
Stiffness	$\overline{K}_{ij} = K_{ij} / K_*$	$K_* = m\,L\,W\left(\frac{D}{2\,c_{min}}\right)^3$
Damping	$\overline{C}_{ij} = C_{ij} / C_*$	$C_* = K_* / W$
Critical mass	$\overline{M} = M_c / M_*$	$M_* = K_* / W^2$

The dimensionless torque remains nearly uniform over the entire speed range, thus indicating a linear dependency on the journal speed. The bearing mechanical power dissipated is 1.2 watts at the highest operating speed. This magnitude is a minute fraction of the mechanical power currently lost with oil lubricated bearings. Figure 3 also depicts the journal attitude angle decreasing as the rotor speeds up. This effect indicates the rising importance of the fluid compressibility and hydrostatic feed as the operating speed increases. Operating eccentricity is relatively small and negligible (centered condition) at high speeds.

Figure 4 displays the calculated profile of the gas film pressure along the circumferential and axial coordinates for two rotor speeds, 0 and 180 krpm. The results for the pure hydrostatic condition show a characteristic circumferential symmetric pressure field with a parabolic shape towards the axial discharge plenum. On the other hand, at the highest speed, the pressure shows a sudden pressure rise and drop at the feed location as a result of the large rotor surface speed, which advects the feed flow downstream of the supply orifice. Note also that the axial pressure profile is more uniform towards the axial ends, a typical characteristic for operation at large compressibility numbers.

Figures 5 depict in dimensionless form the effects of excitation frequency on the bearing stiffness and damping (direct and cross-coupled) force coefficients. The coefficients are graphed as a function of the excitation frequency ratio (w/W) for three rotor speeds noted as LS (30 krpm), MS (90 krpm), and HS (150 krpm). Note that the physical magnitude of the excitation frequencies increases proportionately with the rotor (journal) speed. Unlike in incompressible fluid film bearings, gas bearings evidence strong effects of frequency which lead to a sharp increase in the direct stiffness (K_{xx}) and a dramatic reduction in the direct damping coefficient (C_{xx}). Incidentally, the cross-coupled stiffness coefficient (K_{yx}) also shows a reduction, but at a lower rate than the direct damping, thus leading eventually to the onset of hydrodynamic instability.

At the near centered operation, $K_{yy}=K_{xx}$ and $K_{yx}=-K_{xy}$, Lund [LUN 68] defines equivalent synchronous stiffness and damping coefficients as $K_e=K_{xx} + W C_{xy}$ and $C_e=C_{xx}-K_{xy}/W$, respectively. The critical mass (M_c) indicates the largest possible inertia the bearing may support at the threshold speed of instability (W_c) when considering a simple rigid rotor. Sub synchronous motions with a typical whirl frequency ratio (WFR) characterize the instability. Table 3 presents the physical magnitude of the equivalent parameters, the critical mass and the WFR. The feed orifice diameter was sized to obtain an optimum (zero frequency) hydrostatic stiffness at 150 krpm. However, the bleed pressure available from the compressor discharge is not large enough to generate significant direct stiffness coefficients that will ensure higher rotor-bearing natural frequencies and operation free of sub synchronous motion.

Figure 6 depicts the dimensionless equivalent stiffness and damping coefficients and critical mass versus the bearing speed number. In spite of the hydrostatic

pressurization, the WFR for all operating conditions is ~0.50, as in plain hydrodynamic bearings. The dimensionless results follow closely the trends presented by Lund [LUN 68] for a three-lobe hydrodynamic bearing. Note that the physical parameters show a continuous increase (decrease) of the stiffness (damping) coefficients as the rotor speed increases, and lead to a significant reduction in the critical mass, which becomes lower than the actual TC ½ rotor mass, for rotor speeds above the threshold speed (W_c) of 60 krpm.

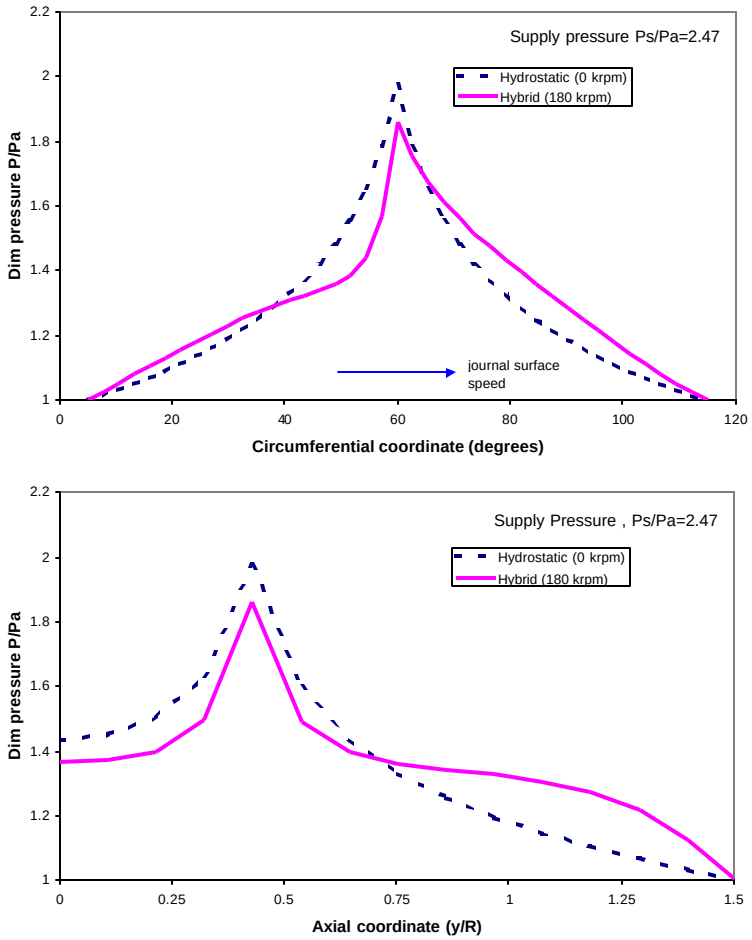

Figure 4. *Pad pressure at orifice plane (a) P/P_a vs. q, (b) P/P_a vs. (y/R) at null and 180 krpm rotor speeds.*

The threshold speed noted is valid for a rigid rotor supported on two identical gas bearings. However, in actual practice the rotor is flexible and the actual threshold speed may be well below the rigid rotor speed limit. The WFR characteristic maintains its magnitude though [CHI 93].

Table 3. *Equivalent synchronous stiffness and damping coefficients, critical mass, and WFR for gas bearing (dimensional values).*

Speed krpm	Speed Number, L_B	K_e N/m	C_e Ns/m	M_c kg	*WFR*
15	1.46	166425	242	0.160	0.50
30	2.96	456266	190	0.106	‘’
45	4.51	715185	154	0.072	
60	6.13	915271	133	**0.050**	limit
75	7.84	1093293	118	0.036	
90	9.65	1251847	109	0.028	
105	11.56	1397309	102	0.022	
120	13.60	1526948	95	0.018	
135	15.75	1639343	90	0.015	
150	18.01	1737666	85	0.013	
180	22.87	1896594	77	0.009	

½ TC rotor mass ~ 0.050 kg

5. Conclusions

Oil Free turbomachinery implementing gas bearings will satisfy stringent environmental constraints, offer near to frictionless operation, improve reliability, and offer substantial savings in component and system weight and complexity. Successful implementation of the technology requires of adequate modeling techniques validated by extensive experimentation and field troubleshooting practice.

A novel finite element formulation for gas bearing analysis is advanced. The method introduces high order weight functions that prevent the need of ad-hoc upwind parameters and non-symmetrical weighting functions, as in the case of the Petrov-Galerkin scheme. The exact weight functions naturally incorporate the flow character, and reduce to the well known bilinear shape functions at low compressibility numbers, or become full-upwind (pure advection) functions for operation at large surface speeds.

The computational FE model forwards predictions of the static performance parameters and dynamic force coefficients of a three-pad hydrostatic/hydrodynamic gas bearing for application to oil-free automotive turbochargers. The dynamic force coefficients are highly dependent on frequency, which leads to a sharp increase in direct stiffness coefficient and a dramatic decrease in the direct damping coefficient. The cross-coupled stiffness coefficient decreases at a lower rate than the direct

damping coefficient, thereby leading to the onset of hydrodynamic instability at rotor speeds well below the design range of operating conditions. Direct air bleed from the compressor discharge provides the external pressurization to the bearing, effective

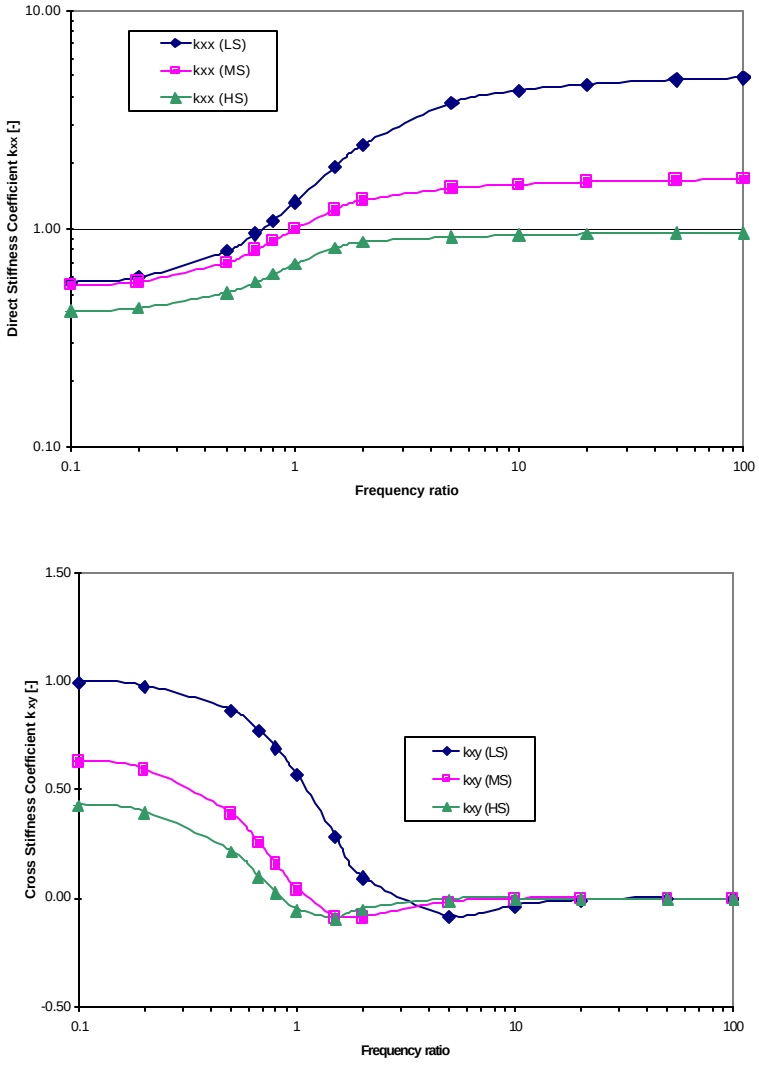

Figure 5a. *Dimensionless direct and cross-stiffness coefficients versus frequency ratio (ω/W) for three rotor speeds. LS (30 krpm), MS (90 krpm), HS (150 krpm).*

at rotor speeds above 75 krpm, thus indicating bearing operation in a hydrodynamic mode at low rotor speeds. The lack of enough pressurization does not allow the generation of higher direct stiffness coefficients that could ensure larger rotor -

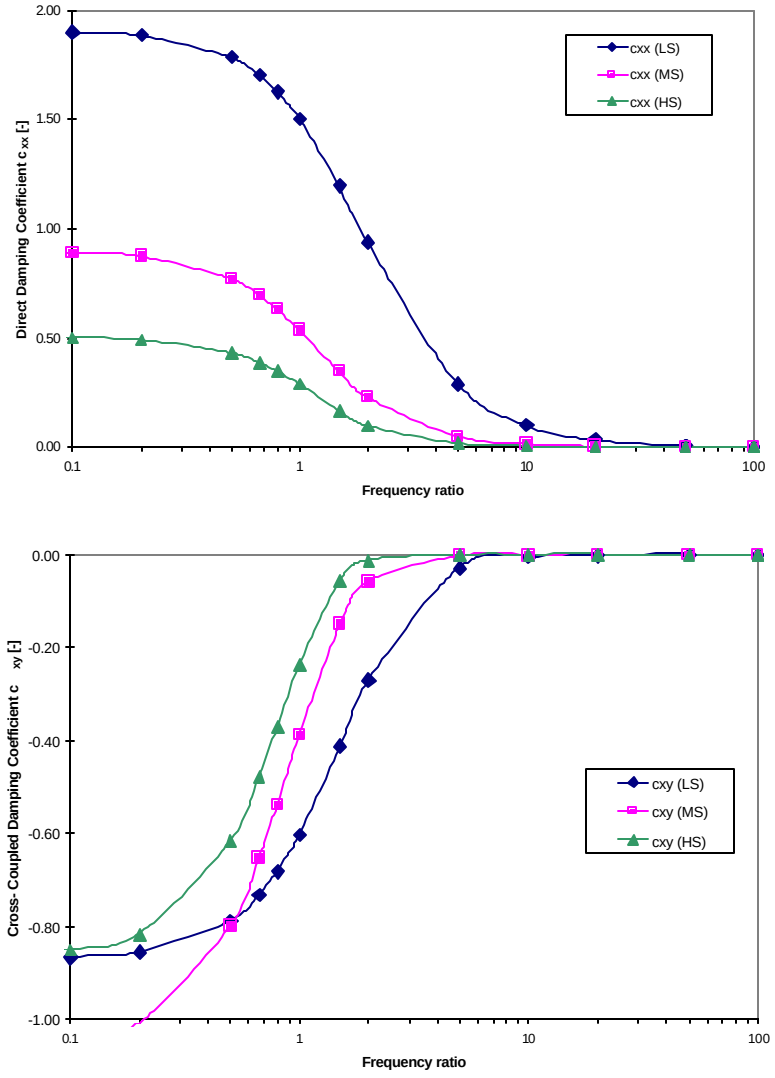

Figure 5b. *Dimensionless direct and cross-stiffness coefficients versus frequency ratio (ω/W) for three rotor speeds. LS (30 krpm), MS (90 krpm), HS (150 krpm).*

bearing natural frequencies and operation free of sub synchronous motion. The gas bearing mechanical power is a minute fraction of the power required by conventional oil-lubricated floating ring bearings.

The FE computational model proves fast, efficient and accurate. Yet, it does not address to those crucial issues known to impact the practical implementation of gas bearings to high speed operation. Little damping is inherent to gas bearings, which in addition must survive intermittent rubs and lack of rotor lift while undergoing frequent startups and shutdowns.

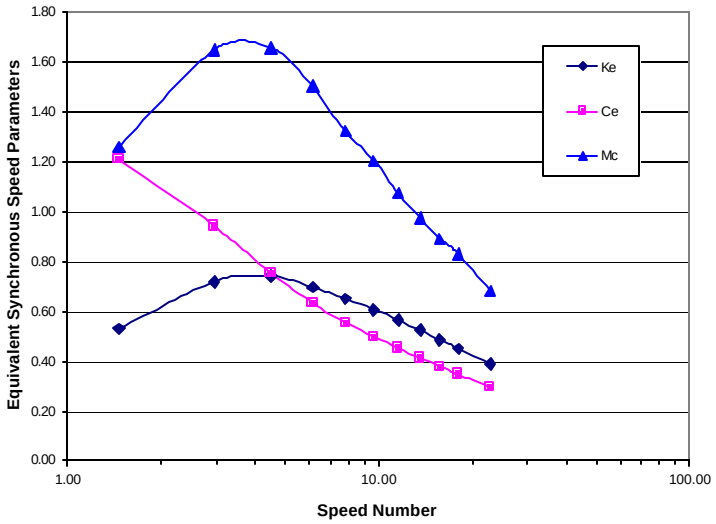

Figure 6. *Dimensionless synchronous stiffness and damping coefficients and critical mass for candidate gas bearing versus Speed (compressibility) number.*

Acknowledgments

The authors acknowledge the financial support of the Texas Energy Resources Program and Garrett Engine Boosting Systems. Thanks to Mr. Gerry LaRue at Garrett for sharing his knowledge on turbocharger design and needs. Thanks to Mr. Thomas Soulas for the translation of the Abstract into French.

Bibliography

[BAT 82] BATHE K.J., *Finite Element Procedures in Engineering Analysis*, Englewood Cliffs, New Jersey, Prentice Hall, 1982.

[CAS 65] CASTELLI V., ELROD H.G., "Solution of the Stability Problem for 360 Deg Self-Acting, Gas-Lubricated Bearings," *Journal of Basic Engineering*, Series D, Vol. 87, No. 1, 1965, pp. 199-212.

[CAS 67] CASTELLI V., VOHR J.H., "Performance Characteristics of Herringbone-Grooved Journal Bearings Operating at High Eccentricity Ratios With Misalignment," Paper No. 14, *Proceedings Gas Bearing Symposium*, University of Southampton, Apr. 1967.

[CAS 68] CASTELLI V., PIRVICS J., "Review of Numerical Methods in Gas Bearing Film Analysis", *ASME Journal of Lubrication Technology*, 1968, pp. 777-792.

[CHI 93] CHILDS D., *Turbomachinery Rotordynamics*, John Wiley & Sons, Inc., 1993.

[CZO 96] CZOLCZYNSKI K., "How to Obtain Stiffness and Damping Coefficients of GasBbearings," *Wear*, Vol. 201, No. 1-2, 1996, pp. 265-275.

[ELR 60] ELROD H.G. Jr., MALANOSKI S.B., Theory and Design Data for Continuous-Film, Self-Acting Journal Bearings of Finite Length, Report I-A 2049-13, Nov. 1960, The Franklin Institute Laboratories for Research and Development.

[ELR 67] ELROD H.G. Jr., MCCABE J.T., CHU T.Y., "Determination of Gas-Bearing Stability Response to a Step-Jump," *ASME Journal of Lubrication Technology*, Vol. 89, No. 9, 1967, pp. 493-498.

[FAR 99] FARIA M.T.C., Finite Element Method of High Speed Grooved Gas Bearings, Ph.D. Dissertation, Texas A&M University, June 1999.

[FAR 00] FARIA M.T.C., SAN ANDRES L., "On the Numerical Modeling of High-Speed Hydrodynamic Gas Bearings," *ASME Journal of Tribology*, Vol. 122, No. 1, 2000, pp. 124-130.

[FAR 01] FARIA M.T.C., "An Efficient Finite Element Procedure for Analysis of High-Speed Spiral Groove Gas Face Seals," *ASME Journal of Tribology*, Vol. 123, No. 1, 2001, pp. 205-210.

[FUL 69] FULLER D.D., "A Review of the State-of-the-Art for the Design of Self-Acting Gas-lubricating Bearings", *ASME Journal of Lubrication Technology*, Vol. 91, No. 1, 1969, pp. 1-16.

[GRO 62] GROSS W.A., *Gas Film Lubrication*, New York, John Wiley & Sons, 1962.

[GUN 64] GUNTER E. J., HINKLE J. G., FULLER D. D., "The Effects of Speed, Load, and Film Thickness on the Performance of Gas-Lubricated, Tilting-Pad Journal Bearings," *ASLE Transactions*, Vol. 7, 1964, pp. 353-365.

[HAM 94] HAMROCK B.J., *Fundamentals of Fluid Film Lubrication*, New York, McGraw-Hill, 1994.

[HEI 77] HEINRICH J.C., HUYAKORN P.S., ZIENKIEWICZ O.C., MITCHELL A.R., "An Upwind Finite Element Scheme for Two-dimensional Convective Transport Equation",

International Journal for Numerical Methods in Engineering, Vol. 11, No.1, 1977, pp. 131-143.

[LUN 64] LUND J.W., "The Hydrostatic Gas Journal Bearing With Journal Rotation and Vibration," *Journal of Basic Engineering*, Trans. ASME, Series D, Vol. 86, No. 2., 1964, pp. 328-336.

[LUN 67] LUND J.W., "A Theoretical Analysis of Whirl Instability and Pneumatic Hammer for a Rigid Rotor in Pressurized Gas Journal Bearings," *Journal of Lubrication Technology, Transactions of the ASME*, April 1967, pp. 154-166.

[LUN 68] LUND J.W., "Calculation of Stiffness and Damping Properties of Gas Bearings," *Journal of Lubrication Technology*, 1968, pp. 793-804.

[MAJ 88] MAJUMDER M.C., MAJUMDAR B.C., "Theoretical Analysis of Pneumatic Instability of Externally Pressurized Porous Gas Journal Bearings Considering Velocity Slip," *ASME Journal of Tribology*, Vol. 110, No. 4, 1988, pp. 730-733.

Nomenclature

a	Orifice restrictor diameter [m]
A	Effective orifice area [m^2]. (πa^2) or $(\pi d h)$
C	Nominal pad clearance [m]
C_{sb}	Damping coefficients; $_{s,b=X,Y}$ [N/m]. $\overline{C}_{sb} = C_{sb} W / K_*$
d	Orifice discharge diameter [m]
D	Journal (rotor) diameter [m]
e_X, e_Y	Journal eccentricity components [m]
f_X, f_Y	$\cos(\theta)$, $\sin(\theta)$. Perturbation circular functions.
F_X, F_Y	Fluid film forces [N]
g	Orifice geometry function. Equation [5].
h	Film thickness [m]. $H=h/C$
$\boldsymbol{i}$	$\sqrt{-1}$. Imaginary unit.
k	Gas specific heat ratio. (1.4 for air). $\gamma=(k-1)/k$
$[k]^e$, $[k]_G$	FE local and global fluidity matrices.
K_{sb}	Stiffness coefficients; $_{s,b=X,Y}$ [N/m] $\overline{K}_{sb} = K_{sb} / K_*$
K_*	Stiffness conversion factor [N/m]. $\mu L W \left(\frac{D}{2 c_{min}}\right)^3$
K_e, C_e	$K_{xx} + W C_{xy}$; C_{xx}-K_{xy}/W. Effective synchronous stiffness and damping coefficients [N/m, N.s/m].
L	Bearing axial length [m].
L_x	Pad circumferential extent [rad]. $[R(\theta_t - \theta_l)]$
M_c	Rigid rotor critical mass [kg]. $\overline{M}_c = M_c W^2 / K_*$
$\dot{m}$	Mass flow rate [kg/s].

N_{em}	$\left(N_x^e \times N_y^e\right)$ Number of elements in flow domain.
N_{pad}	Number of pads.
P	Gas absolute pressure [Pa]. $p = P / P_*; \overline{P} = P / P_s$
P_0, P_s	Zeroth- and first-order pressure fields. [Pa], $_{s\ =X,\,Y}$ [Pa/m]
$\{q\}^e$, $\{Q\}_G$	FE local and global nodal flow vectors
$\{r\}^e$, $\{R\}_G$	FE local and global shear-squeeze vectors
r_p	Pad preload [m]
R	Journal radius, [m]. $\left(D/2\right)$
$\Re_g$	Gas constant [J/kg · K]
t	Time [s]
T	Absolute temperature [K]
T_{orq}	Bearing torque [Nm]
W	Applied load, $\sqrt{F_X^2 + F_Y^2}$
$x= R\theta, y$	Coordinate system on plane of bearing. $\{\overline{x}, \overline{y}\} = \{x, y\} / L_x$
X, Y	Inertial coordinate system
Z_{sb}	Impedance coefficients, $\left(K_{sb} + \mathbf{i}wC_{sb}\right)$; $_{s,\,b\,=X,\,Y}$ $\left[\mathrm{N}/\mathrm{m}\right]$
a'	Non-isentropic loss coefficient
D	Feed orifice geometric ratio, $D=a^2/dC$
d_{OR}	Dimensionless orifice parameter. $\dfrac{p\,a^2}{A}\dfrac{12\mu L_x^2}{C^3\left(P_* r_*\right)^{1/2}}\,p_s$
θ, Q	Circumferential coordinate. Pad angular coordinate [rad].
L	Pad speed (compressibility) number. $\dfrac{6\,\mu W R L_x}{C^2 P_*}$
l_e	Local Peclet number on FE. $l_e = \dfrac{L\,l_x^e}{p_0^e H_e^2}$
μ	Gas viscosity [Pa · s]
ξ, η	FE natural coordinates
ρ	Gas density [kg /m^3]
σ	Excitation frequency number. $\dfrac{12\,\mu w\ L_x^2}{C^2 P_*}$
τ	Dimensionless time, ωt
Φ	$\sqrt{\Re_g T}\,\dfrac{p\,a^2}{A}\,P_s$. Orifice factor [Pa.m/s]
ϕ	Journal attitude angle [rad]. $tg^{-1}\,(-F_{Yo}/F_{Xo})$.
$\{y_i^e\}_{i=1..4}$	FE shape (weight) functions
Ω, ω	Journal rotational speed and excitation frequency [rad/s].
Ω^e, G^e	FE element and boundary

Subscripts

a, s	Ambient and supply conditions
e	Finite element. Effective value.
G	Global
l,t, p	Pad leading, trailing and offset positions.
OR	Orifice
0	Zeroth order field
a , b	*X, Y.* First order fields, direction of perturbation
*	Characteristic value at ambient conditions

Appendix I: title of the paper in french

Analyse par éléments finis de paliers à gaz pour turbomachines fonctionnant sans huile

Appendix II: validation of FE model with published results

Lund [LUN 68] presents design charts for the synchronous force coefficients and critical mass parameter of cylindrical gas bearings for application to vertical (no load) rotating machinery. Lund's charts are routinely used to extract the dimensions of a particular bearing design or to estimate the critical mass (stability limit) of a point mass rotor mounted on a gas bearing.

Lund implemented a finite difference computational program to prepare the design charts. Figure A depicts the FE predictions for the synchronous effective force coefficients, critical mass, and drag torque for a three lobe (hydrodynamic) bearing with slenderness ratio L/D=1, pad arc length of 100°, and preload ratio (r_p/C) of 50%. The operating conditions are ambient, i.e. P_a=1 bar (r =1.27 kg/m^3, m=1.9 10^{-5} Pa.s). The parameters are shown in dimensionless form versus Lund's bearing speed number. See the Nomenclature for the parameters appropriate definition.

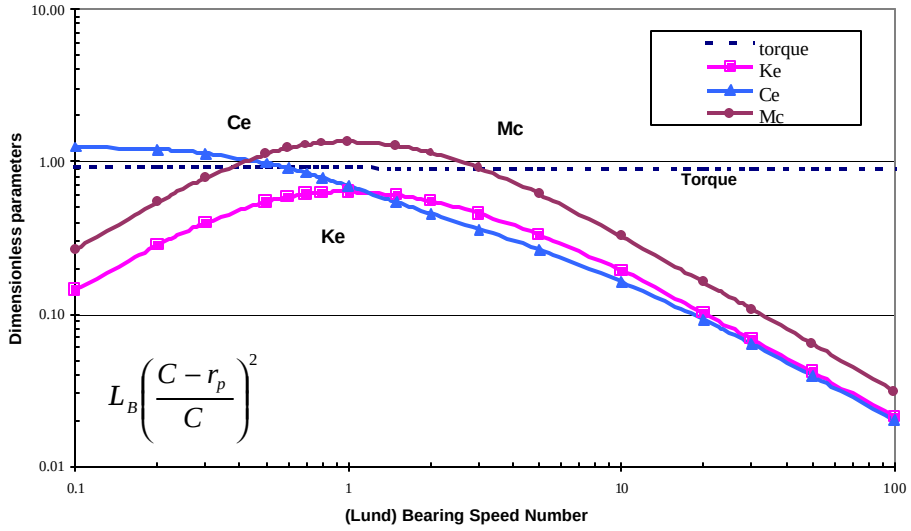

Figure A. *Dimensionless synchronous stiffness and damping, critical mass, and torque for three pad (100 deg arc) hydrodynamic gas bearing. L/D=1, rp/C=0.***5**

The FE results in Figure A reproduce exactly those advanced by Lund. The current results, however, extend the predictions to a higher speed bearing number $D_B\left(C - r_p / C\right)^2$, one order of magnitude larger than the maximum value reported by Lund. The FE results, obtained with $N_x \, x \, N_y$=41 x 9 elements on each bearing pad, demonstrate the model accuracy and its robustness for applications to large bearing speed numbers.